Journal of Applied Fluid Mechanics, Vol. 18, No. 5, pp. 1285-1300, 2025.
Available online at www.jafmonline.net, ISSN 1735-3572, EISSN 1735-3645.
https://doi.org/10.47176/jafm.18.5.3037

Research on the Influence of Jet Control Point Distribution on Gas–liquid Separation Characteristics in a Helical Axial-flow Multiphase Pump

P. Qiang[1†], R. Li[1,2], W. Han[1,2], Y. Fu[1,2] and S. Zhang[1,2]

[1] *School of Energy and Power Engineering, Lanzhou University of Technology, Lanzhou, Gansu, province, 730050, China*
[2] *Key Laboratory of Advanced Pumps, Valves and Fluid Control System of the Ministry of Education, Lanzhou University of Technology, China*

†*Corresponding Author Email: 231080704010@lut.edu.cn*

ABSTRACT

Helical axial-flow multiphase (HAFM) pumps experience intermittent gas-blocking events, which negatively impact performance and threaten the stability of the overall pump and pipeline systems. This study applies jet flow field method to HAFM pumps. Active intervention in the gas-liquid separation process, utilizing external energy, results in the reorganization of the flow field within HAFM pumps. The effect of jet location on improving the efficiency of HAFM pumps is assessed, with a focus on the active flow control mechanism through jet influence. The study indicates that the region sensitive to jet site distribution affecting pump performance is $0.5L_c \leq x_r \leq 0.7L_c$, while the weakly sensitive region is $0.15L_c \leq x_r \leq 0.5L_c$. When $x_r \leq 0.15L_c$, the improvement in head and efficiency under high gas content conditions is reduced. Jet flow field control technology obviously decreases the gas phase accumulation in the downstream flow channel of the moving blade cascade. The optimal position for reducing gas phase agglomeration in the impeller channel is $0.3L_c$. The jet site arrangement significantly affects the pressure structure near the cascade trailing edge. Appropriate jet hole positioning significantly improves the pressure structure at the cascade trailing edge, decreases reflux caused by separation vortices at the impeller outlet, and enhances the hydraulic performance in the multiphase pump.

Article History

Received July 30, 2024
Revised December 17, 2024
Accepted December 19, 2024
Available online March 4, 2025

Keywords:

Active jet
Gas–liquid mixed transport
Gas phase aggregation
Helical axial-flow multiphase pump
Jet position

1. INTRODUCTION

Global consumption of oil and natural gas, highlighting their role as major energy sources worldwide, has exceeded 300 exajoules annually since 2014 (EI, 2023). As oil and gas reserves in onshore and shallow-water regions decline and degrade, exploration and development have shifted to deep-sea and deep-ground environments (Chang & Wang, 2024). Deep-sea oil and gas extraction is technically challenging and capital-intensive. Oil and gas mixed transportation technology can replace costly offshore oil and gas development platforms, reduce investments in separation devices, simplify pipeline configurations, lower construction costs, and improve offshore development efficiency.

The HAFM pump serves as the critical booster device for extracting oil and gas from deep-sea environments. When media of different densities are mixed and transported within the pump, gas–liquid separation occurs due to centrifugal forces. When the gas content in the pump is relatively high, the gas–liquid separation will be very significant, and the separated gas phase will intermittently accumulate at the rotor cascade trailing edge, thereby blocking the impeller channel. This leads to large periodic fluctuations in the pump outlet pressure, which seriously threatens the safety of the pump unit and pipeline system. Understanding the interfacial forces between two phases is crucial to analyzing the gas–liquid separation mechanism. Yu et al. (2015) analyzed the interfacial forces in the impeller region of a HAFM pump and found that drag force was dominant under different inlet gas content rates, bubble diameters, and impeller speeds. Zhang et al. (2018) discovered that drag force is the most significant interfacial force in gas–liquid two-phase pumps, followed by the added mass and lift forces. Increasing inlet gas content strengthens interfacial forces. Based on the Euler model， Suh et al. (2018) optimized

NOMENCLATURE

C_{jet}	jet velocity coefficient
c_t	tip clearance
D_d	guide vane shroud diameter
D_t	impeller shroud diameter
D_{jet}	jet hole diameter
d_{h1}	impeller hub inlet diameter
d_{dh1}	guide vane inlet diameter on hub
d_{dh2}	guide vane outlet diameter on hub
E_{jet}	the initial energy of the jet fluid
$E_{Q,R}$	random uncertainty in flow measurements
$E_{H,R}$	random uncertainty in head measurements
$E_{\eta,R}$	random uncertainty in efficiency measurements
$E_{Q,S}$	random uncertainty in flow measurements
$E_{p,S}$	systematic uncertainty in pressure measurements
$E_{M,S}$	systematic uncertainty in torque measurements
$E_{H,S}$	systematic uncertainty in head measurements
$E\eta_{,S}$	systematic uncertainty in efficiency measurements
E_H	combined uncertainty in head measurement
E_η	combined uncertainty in efficiency measurement
e	impeller axial length
e_d	guide vane axial length
F_{fs}, F_{sf}	additional interphase forces
$\boldsymbol{g}$	gravitational acceleration vector
H	head
H_{jet}	pump head for jet scheme
Km	mechanical efficiency constant
Kv	volumetric efficiency constant
L_c	airfoil chord length
L_{imp}	impeller axial length
M	torque
N	number of measurements
n	rotational speed
n_s	pump specific speed
p	static pressure
P_{jet}	power for jet scheme
Q	flow rate
Q_d	design flow rate
Q_{jet}	jet flow rate
S	distance between center of jet hole and suction side of blade
S_x	area of the analysis region
S_X	standard deviation
$S_{x,\ GVF>0.9}$	area of analysis region where the GVF ＞90%
t	time
t_{N-1}	confidence coefficient
$\boldsymbol{u}$	velocity tensor
v_{jet}	jet velocity
v_m	pump meridional velocity
X_a	mean value of the data
x_r	distance between jet hole and trailing edge of blade
Z	number of impeller blades
Z_d	number of guide vane blades

Greek symbols

α	volume fraction
α_{jet}	angle between the projection of the jet direction in the spanwise plane and the tangential line of the suction surface
β	interphase momentum exchange coefficient
β_1	impeller inlet blade angle
β_2	impeller outlet blade angle
β_{d1}	guide vane inlet blade angle
β_{d2}	guide vane outlet blade angle
γ	half cone angle of the hub
γ_{jet}	angle between the jet hole direction and the tangential direction of the hub
λ	gas phase aggregation degree for jet scheme
λ_{jet}	gas phase aggregation degree
η	overall efficiency
η_{jet}	overall efficiency for jet scheme
η_m	mechanical efficiency
η_v	volumetric efficiency
ρ	density
τ	stress tensor
ω	rotational speed of impeller

Subscripts and superscript

l	liquid phase
s	gas phase
in	inlet
out	outlet
β	interphase momentum exchange coefficient
mix	mixture
ori	original pump
*	relative growth rate

Abbreviations

IGVF	Inlet Gas Phase Volume Fraction
GVF	Gas Volume Fraction
HAFM	helical Axial-Flow Multiphase
Span	blade height
SS	Suction Surface
PS	Pressure Surface

the gas-liquid interaction model to improve the accuracy of numerical simulation of HAFM pumps, taking into account various factors such as bubble diameter and force coefficient at the gas-liquid interface. Wen et al. (2024) studied the impact of blade tip clearance on the energy conversion capacity of the HAFM pumps under different

gas volume fractions (GVF). They analyzed the energy conversion behavior and the influence of GVF on energy dissipation and efficiency. Through visualization experiments, Gundersen et al. (2023) observed that tip leakage induces backflow in the impeller and guide vanes. Shi et al. (2020) indicated that the energy transformation capability of a HAFM pump progressively increased from the blade inlet to a 60° blade wrap angle, then decreased due to intensified gas–liquid phase separation. These studies indicate logical connections among gas and liquid interfacial forces, gas–liquid separation, and energy transport in multiphase pumps, providing essential perspectives for the understanding of the working mechanisms of multiphase pumps.

In-depth research on gas–liquid two-phase flow mechanisms has provided extensive theoretical guidance for optimizing and enhancing multiphase pump performance (Dehghan et al., 2024). Researchers have extensively studied methods to enhance gas-liquid performance in multiphase pump impellers. Through visualization experiments, Serena and Bakken (2015, 2016) found that during high-speed operation, the gas phase and liquid phase medium in the impeller are subjected to shear forces, making the distribution more uniform and less prone to separation and gas-phase accumulation. Ejim et al. (2024) also found that with uniform gas–liquid mixing at boundary, gas–liquid separation was lower during high-speed operation in the impeller. Han et al. (2023) and others utilized curved and twisted blades to adjust the forces on the gas phase within impeller channels, alter the gas–liquid separation characteristics, and optimize the pressure structure. Zhou et al. (2023) designed blades for HAFM pumps with separate airfoil trailing edges. By altering the angle and segment length of the blade's rear section, the pressure structure in the region nearby trailing edge of the blades alters the gas-phase retention within the impeller and improves pump performance. These studies demonstrated that optimizing the impeller structure to change the gas–liquid separation characteristics within the flow channel can effectively enhance multiphase pump performance.

End-wall jet technology is a common measure to control the corner separation of compressors， effectively mitigating or removing corner separation, enhancing the compressors' stable operating range (Li et al., 2024). Experimental and simulation results showed that the placement of steady jet holes obviously altered the morphology of the energy loss vortex structure (Meng et al., 2020, 2021). Meanwhile, Yu et al. (2018) found that end-wall jets are highly effective in reducing low-energy fluid accumulation in corner areas, particularly when the jet is positioned at the starting point of corner separation. Wang et al. (2017, 2022) studied the impact of jets on the flow field of subsonic and transonic axial compressors, finding that tip injection reduces the blockage in blade channels, significantly improves the total pressure ratio of compressors, and enhances their stability. Zhao (2023) applied jet technology to improve the stability and cavitation performance of axial-flow pumps, discovering that jets effectively alleviate tip blockage. Jet technology shows significant potential for improving flow performance, offering new thinking and methods about controlling the internal flow field of gas-liquid mixed transport pump.

This study applies jet technology to a HAFM pump. By intervening in gas-phase aggregation on the hub and blade back with jets, intermittent gas-phase accumulation and blockage nearby the rotor blades' trailing edge are alleviated. This is of great significance for enhancing multiphase pump operational stability and realizing large-scale application of HAFM pumps in deep-sea oil and gas exploitation projects. This study compares the effects of different jet hole arrangements on flow field intervention to identify the optimal jet hole configuration, providing a reference for subsequent related studies and engineering applications.

2. PUMP MODEL AND COMPUTATIONAL METHODS

2.1 Pump Model

The HAFM model pump unit, consisting of four main parts as shown in Fig. 1, served as the study object. The model design parameters are listed in Table 1. The blades in the model pump use a 791 airfoil with the key geometric parameters listed in Table 2.

2.2 Mesh Division and Numerical Calculation Methods

Fluent Meshing software was used to complete the spatial discretization for pump fluid domain. Polyhedral meshes with a maximum cell size of 5 mm were applied globally. To capture fluid flow details more accurately, the meshes in the impeller and guide vane regions were locally refined with the maximum cell size limited to 2 mm. For the near-wall region flow, a near-wall modeling method similar to the enhanced wall function approach was used. To ensure turbulence model accuracy, the boundary layer near the wall was set to 12 layers, with a first-layer thickness of 0.01 mm and a growth rate of 1.12, while the Y^+ value was controlled within 5. Steady numerical simulations were performed using the Fluent 2023R1

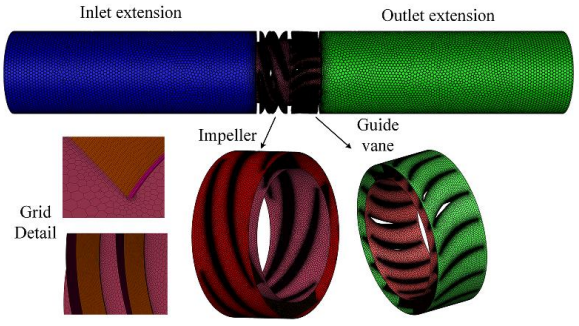

Fig. 1 Schematic diagram of grid division

Table 1 Pump design parameters

Parameter	Value
Designed flow rate Q	50m³/h
Designed Head *H*	10m
Rotation speed *n*	3000r/min
efficiency η	63%
specific speed n_s	230

Table 2 Main parameters of impeller and guide vane

Hydraulic parts	Structural parameter	Value
Impeller	Shroud diameter D_t	136mm
	Hub inlet diameter d_{h1}	100mm
	Axial length e	55mm
	Half cone angle of the hub γ	6°
	Inlet angle of the blade β_1	10°
	Outlet angle of the blade β_2	14°
	Blade number Z	4
	Tip Clearance c_t	0.1mm
Guide Vane	Shroud diameter D_d	136mm
	Hub inlet diameter d_{dh1}	110mm
	Hub outlet diameter d_{dh2}	100mm
	Axial length e_d	50mm
	Inlet angle of the blade β_{d1} /	40°
	Outlet angle of the blade β_{d2}	90°
	Blade number Z_d	17

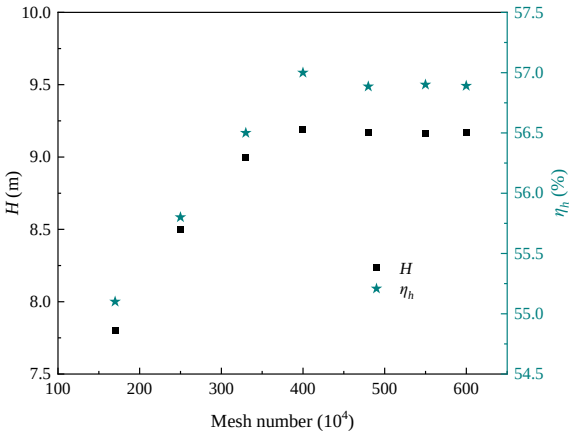

Fig. 2 Mesh irrelevance check

software. Based on prior research by the group, mesh independence was analyzed from hydraulic performance parameters fluctuations with gas content of 20%, as shown in Fig. 2. Head and hydraulic efficiencies were calculated using the following equations:

$$\rho_m = (1-\alpha)\rho_l + \alpha\rho_s \tag{1}$$

$$H = \frac{p_{out} - p_{in}}{\rho_{mix} g} + \frac{v_{out}^2 - v_{in}^2}{2g} \tag{2}$$

$$\eta_h = \frac{\rho_{mix} gQH}{M\omega} \tag{3}$$

In the equations, α-gas volume fraction, p_{in} - inlet static pressures of the pump, p_{out} - outlet static pressures of the pump, ρ_{mix}-density of the mixed medium, M-impeller torque, ω - angular velocity.

It can be observed that beyond 4.8 million grid cells, the head and hydraulic efficiency changes tend to stabilize. Based on the above analysis, the model in this paper adopts about 4.8 million mesh count in the numerical simulation, with 2.80 million meshes for the impeller and 1.74 million for the guide vane.

The Euler–Euler two-fluid model was used to simulate the gas–liquid flow in a HAFM pump. In this model, the gas and liquid phases have separate control equations, with inter-phase transfer terms achieving phase interactions. Compared to the mixture model, the Euler model can more accurately calculate the flow field and is widely used in two-phase flow simulations (Benhmidene, et al. 2011 & Situ et al. 2011). The continuity equations and momentum equations for each phase (Wang, 2020) are as follows.

$$\frac{\partial}{\partial t}(\rho_l \alpha_l) + \nabla \cdot (\alpha_l \rho_l \boldsymbol{u}_l) = 0 \tag{4}$$

$$\frac{\partial}{\partial t}(\rho_s \alpha_s) + \nabla \cdot (\alpha_s \rho_s \boldsymbol{u}_s) = 0 \tag{5}$$

$$\frac{\partial}{\partial t}(\alpha_l \rho_l \boldsymbol{u}_l) + \nabla \cdot (\alpha_l \rho_l \boldsymbol{u}_l \boldsymbol{u}_l) = -\alpha_l \nabla p + \alpha_l \rho_l \boldsymbol{g} + \nabla \cdot \boldsymbol{\tau}_l + \beta(\boldsymbol{u}_s - \boldsymbol{u}_l) + \boldsymbol{F}_{sl} \tag{6}$$

$$\frac{\partial}{\partial t}(\alpha_s \rho_s \boldsymbol{u}_s) + \nabla \cdot (\alpha_s \rho_s \boldsymbol{u}_s \boldsymbol{u}_s) = -\alpha_s \nabla p + \alpha_s \rho_s \boldsymbol{g} + \nabla \cdot \boldsymbol{\tau}_s + \beta(\boldsymbol{u}_l - \boldsymbol{u}_s) + \boldsymbol{F}_{ls} \tag{7}$$

The meanings of all characters in the equations can be found in nomenclature and will not be repeated here.

The SST k-ω turbulence model, which was widely verified (Dehghan & Shojaeefard, 2022; Li et al., 2023; Dehghan & Shojaeefard, 2024; Li et al., 2025), was used, which can ideally predict flow separation phenomena with adverse pressure gradients and effectively predict flow separation points and regions. These models have been widely applied in gas–liquid multiphase pump research, and comparisons with experimental results have confirmed their applicability in this research field (Menter,

1994; Han et al., 2020). The freeze-rotor model was used to handle the moving–static interface (Wang, 2020) with the impeller used a rotating coordinate system, whereas the rest parts used static coordinate system. This model offers excellent stability and high computational efficiency. In two-phase flow calculations, where stability issues and divergence are common, using the frozen rotor model can greatly improve computational efficiency. The inlet is set as the velocity inlet and the outlet is set as free outflow, and the wall is no-slip surface. The calculation residual was set to 10^{-4}.

2.3 Numerical Simulation Validation

The head and efficiency of the pump were calculated using Equations (1)– (3).

To obtain performance parameters, a test bench for a HAFM pump with the structural layout shown in Fig. 3 was built. The test system included a model pump, pipelines for liquid and gas, gas–liquid mixing device, flow meters, valves, and other accessories. During the two-phase flow test, an air compressor supplied the gas. The gas with high pressure exited the air compressor, passed through an air buffer tank for pressure stabilization, and was then injected into the gas–liquid mixing device to mix thoroughly with the liquid phase. Electromagnetic valves were installed on the air buffer and liquid storage tanks outlet to adjust the gas–liquid ratio at the pump inlet, thereby determining the inlet gas content. The flow rate of the gas phase is measured by a vortex flow meter and an electromagnetic flow meter is used to acquire the flow rate of the water. The accuracy of both flowmeters is 0.5%. After being entirely mixed in the gas-liquid mixing apparatus, the gas-liquid mixture flows into the HAFM pump for pressurization and output. The inlet and outlet pipelines of the pump are equipped with pressure gauges with a pressure transmitter accuracy of ±0.2%, which can measure the pressure of the medium before and after pressurization. The motor input torque is measured by a torque sensor with an accuracy of ±0.5%. Figure 3(b) shows a schematic diagram of the test bench. In the diagram, orange represents the pipeline for transporting the liquid phase, blue represents the pipeline for transporting the gas phase, and green represents the pipeline for transporting the gas–liquid mixture.

Experimental uncertainty considers both random and systematic uncertainties (Guan, 2011). The random uncertainty equation is:

$$E_R = \pm \frac{t_{N-1} S_X}{X_a \sqrt{N}} \times 100\% \tag{8}$$

In the equation, N is the number of measurements; t_{N-1} is the confidence coefficient, which is 2.23 for ten measurements (Guan, 2011); S_X is the standard deviation of the N measurement results, and X_a is the average of the N measurement results. By calculation, the random uncertainties of flow rate Q, head H, and efficiency η are obtained as follows: $E_{Q,R}= \pm 0.144\%$, $E_{H,R}=\pm 0.084\%$, $E_{\eta,R}=\pm 0.173\%$.

According to the accuracy of the measuring instruments selected for the experiment, the systematic

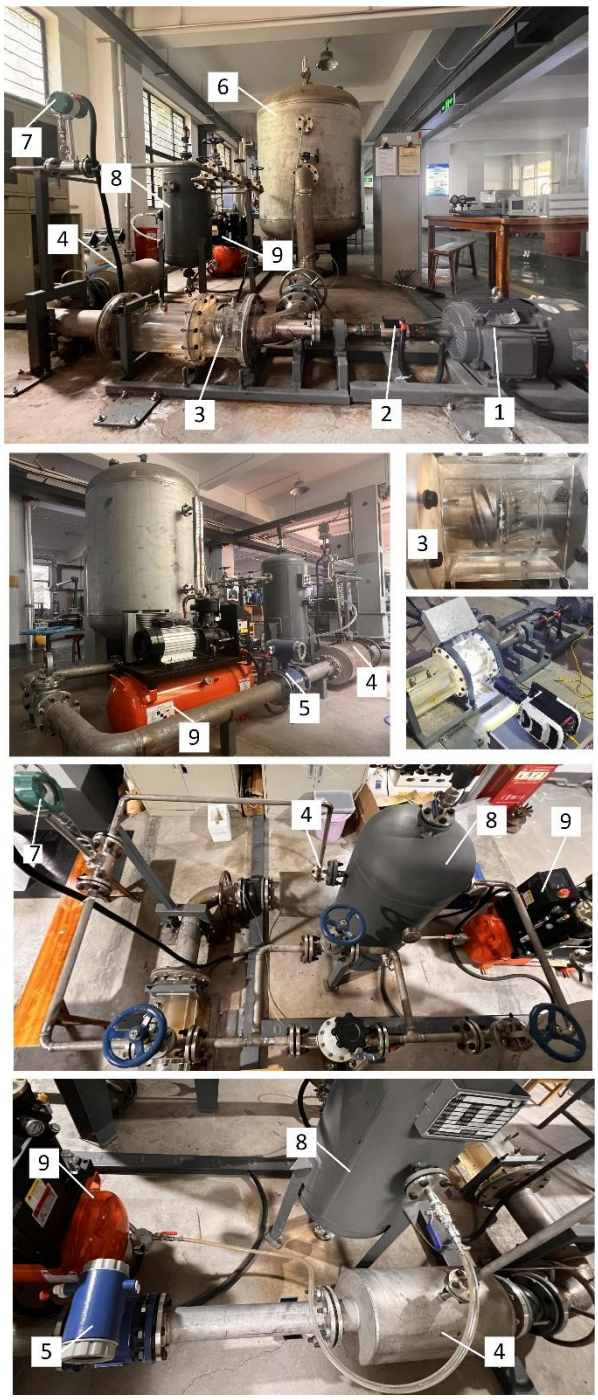

(a) Photos of test bench layout

(b) Schematic flow of the test bench

Fig. 3 Pump experimental system. 1 Motor, 2 Torque mete, 3Visualization region, 4 Gas–liquid mixing apparatus, 5 Electromagnetic flow meter, 6 Liquid storage tank, 7Vortex flow meter, 8Air buffer tank, 9 Air compressor

uncertainties of the flow meter, pressure sensor, and torque sensor are as follows: $E_{Q,S}$=±0.5%, $E_{p,S}$=±0.2%, $E_{M,S}$=±0.5%. The systematic uncertainties of the head and efficiency are as follows:

$$E_{H,S} = \sqrt{E_{p,S}^{\ 2} + E_{p,S}^{\ 2}} = 0.28\% \tag{9}$$

$$E_{\eta,S} = \pm\sqrt{E_{Q,S}^{\ 2} + E_{H,S}^{\ 2} + E_{M,S}^{\ 2}} = \pm 0.76\% \tag{10}$$

In summary, the combined uncertainties of the measured pump parameters are as follows:

$$E_H = \sqrt{E_{H,R}^{\ 2} + E_{H,S}^{\ 2}} = \pm 0.29\% \tag{11}$$

$$E_\eta = \sqrt{E_{\eta,R}^{\ 2} + E_{\eta,S}^{\ 2}} = \pm 0.779\% \tag{12}$$

The model pump experiments were conducted on the HAFM pump using gas–liquid mixtures as the medium under flow conditions ranging from 0.8Q_d to 1.3Q_d. In the gas–water two-phase flow experiment conducted on the test platform constructed by the authors' group, when the IGVF was low, the gas-phase distribution at the pump inlet was more uniform, resulting in a better match with the numerical simulation inlet conditions. Based on previous experimental results of the research group, the experimental results under an inlet gas content of 10% were compared with the numerical simulation results, as shown in Fig. 4.

Figure 4 shows that the numerical calculation results for the head and hydraulic efficiency exhibit the same trend as the experimental head and efficiency with changing flow rates. The average relative error of the head is 6.0%, with a deviation of 5.6% at the design point. The average relative error between the experimental and simulated hydraulic efficiencies was 5.8%, with a deviation of 5.0% at the design point. Because the numerical simulations neglect volumetric and mechanical losses, the discrepancies between the numerical and experimental results were within an acceptable range. The total efficiency of the pump is the product of hydraulic efficiency, mechanical efficiency, and volumetric efficiency. However, since numerical simulation methods

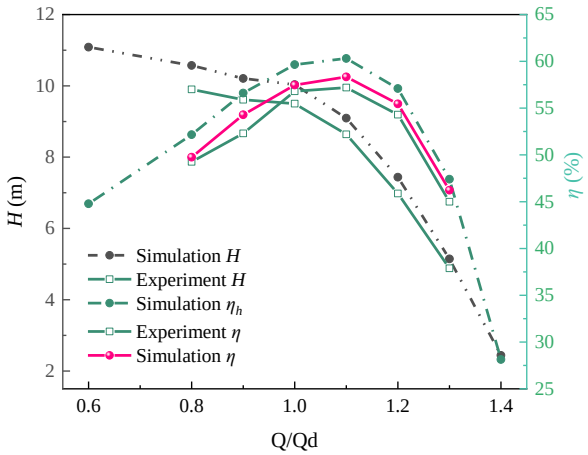

Fig. 4 Comparing simulation results with experimental data.

cannot simulate mechanical efficiency, the total efficiency cannot be directly obtained the total efficiency cannot be directly obtained through simulation. To ensure consistency in using total efficiency when comparing simulation results with experimental results, estimations of mechanical efficiency and volumetric efficiency are required. As the helical axial-flow pump does not have disk friction losses, the mechanical efficiency only accounts for bearing and packing losses, which are typically very small. According to the recommended values from Guan (2011), the mechanical efficiency is generally between 0.97 and 0.99. In this study, the estimated mechanical efficiency under design conditions is taken as ηm,d=0.98.The volumetric efficiency under design conditions is estimated using the centrifugal pump volumetric efficiency estimation method, as shown in Equation (13) (Guan, 2011). The mechanical efficiency and volumetric efficiency for different operating conditions are calculated using Equations (14-15) (Yan et al., 2007).

$$\eta_{v,\ d} = 1/(1+0.68n_s^{-2/3}) \tag{13}$$

$$\eta_v = Q/(Q+K_vH^{1/2}) \tag{14}$$

$$\eta_m = 1-K_m\eta_{m,d}/Q \tag{15}$$

In the equations, Km=1, and Kv=0.28.

Using the above method, the total efficiency from numerical simulations was estimated and compared with the experimental results. It was found that the average relative error between the experimental efficiency and the simulated total efficiency was 2.14%, while the deviation between the experimental and simulated total efficiency at the design operating point was 1.17%. The two results are very close. These outcomes indicate that the numerical simulation method utilized is suitable and produces highly accurate results, strongly endorsing the credibility of this research.

2.4 Jet Scheme Design

In a HAFM pump, mixed media experience varying centrifugal forces due to density differences. As the impeller rotates, the lighter gas phase aggregates near the hub side owing to the centrifugal forces, with the denser water phase flowing toward the shroud side. The impeller，as a pressurizing component，inevitably creates a reverse pressure gradient within its flow passage. An adverse pressure gradient causes the gas phase to accumulate and even stagnate near the impeller blade trailing edge, resulting in gas lock and blockage phenomena. Jet techniques aim to replenish energy for the gas phase retained within the impeller using high-speed jets. Jet energy entrainment and intervention help mitigate the aggregation of the gas phase in the low-pressure position of the flow channel thereby reducing the blockage caused by the retained air masses in the impeller. The effectiveness of the flow intervention is strongly relevant to the positions of jet holes.

Gas retention commonly occurs on the blade surfaces, where gas-liquid separation is more pronounced. All jet structures were positioned on the suction side of the blades

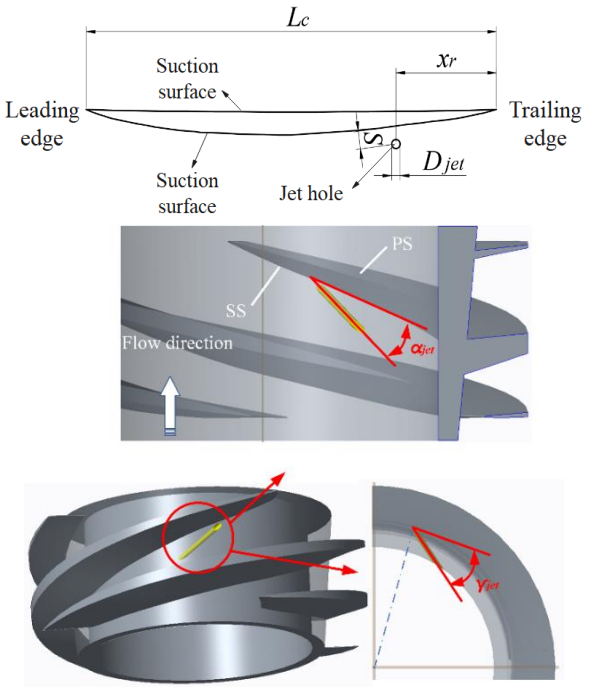

Fig. 5 Schematic of jet hole locations

Table 3 Jet hole arrangement schemes

Serial Number	Scheme Name	Number of Holes	Hole Position / (x_r/L_c)
0	$Case_{ori}$	/	/
1	$Case_{1.a}$	1	0.7
2	$Case_{1.b}$	1	0.5
3	$Case_{1.c}$	1	0.3
4	$Case_{1.d}$	1	0.15
5	$Case_{2.a}$	2	0.3/0.15
6	$Case_{2.b}$	2	0.15/0.075

to avoid disrupting the pressure side. Four jet hole positions were selected in this study: $0.15L_c$, $0.3L_c$, $0.5L_c$, and $0.7L_c$ from the blade trailing edge. Six jet hole arrangement schemes were designed, detailed in Table 3. All schemes used circular jet holes with a diameter of D_{jet}=1 mm, centered S=1 mm from the low-pressure surface of blade. The angle γ_{jet} between the jet hole direction and the tangential direction of the hub is set to 15°, and the angle α_{jet} between the projection of the jet direction in the spanwise plane and the tangential line of the suction surface (SS) airfoil profile is 5°, oriented toward the low-pressure surface of blade. A schematic of the jet holes is shown in Fig. 5.

Based on the author's prior research, all the above jet schemes used a jet velocity coefficient of $C_{jet}=v_{jet}/v_m$ =10, where v_{jet} is the jet velocity, and v_m is the pump meridional velocity.

3. RESULTS

3.1 Influence of Jet Location Distribution on Performance

With the jet fluid involved, the energy increment within the pump includes the energy acquired by the fluid entering the pump inlet and the additional energy supplied by the jet fluid. Additionally, the calculation of the input power must account for the initial energy supplied by the jet. The efficiency that accounts for energy change due to the jet fluid is referred to as the pump net hydraulic efficiency (Hereafter as pump efficiency), denoted by η_{jet}. The formula is:

$$\eta_{jet}=\frac{(p_{out}-p_{in})Q+\Delta p_{jet}Q_{jet}}{M\omega+E_{jet}} \tag{16}$$

p_{out} - total pressure at the pump outlet, p_{in} - total pressure at the pump inlet, Q -pump inlet flow rate, Q_{jet} -jet flow rate, E_{jet} - original energy of the jet fluid.

To assess the effect of jet position on the multiphase pump performance.

$$\eta_{jet}^{*}=\frac{\eta_{jet}-\eta_{ori}}{\eta_{ori}}\times 100\% \tag{17}$$

$$H_{jet}^{*}=\frac{H_{jet}-H_{ori}}{H_{ori}}\times 100\% \tag{18}$$

$$P_{jet}^{*}=\frac{P_{jet}-P_{ori}}{P_{ori}}\times 100\% \tag{19}$$

where H_{jet}, P_{jet}, η_{jet} are the performance indicators of the scheme with the jet structure, and H_{ori}, P_{ori}, η_{ori} are the performance indicators of the prototype pump. The head, shaft power, and net efficiency of the pump at different jet positions are shown in Fig. 6**.**

Changing the jet injection position significantly affected the performance of the HAFM pump and with a more pronounced effect at higher inlet gas volume fractions (IGVF).

From Fig. 6(a) and (b), which show the changes in the pump efficiency for different jet positions, it is observed that under IGVF = 0, the pump efficiency of all jet schemes is lower than that of the prototype pump. When IGVF > 0, pump efficiency increases, becoming more significant as the IGVF rises. The jet control strategy does not remedy the pump flow field under pure liquid conditions but enhances the flow under gas–liquid mixed conditions, showing that jet control mainly impacts gas-phase flow conditions.

Comparing the single-hole jet schemes $Case_{1.a}$, $Case_{1.b}$, $Case_{1.c}$, and $Case_{1.d}$, it is found that under IGVF ≥ 0.2 conditions, the closer the jet hole is to the blade's trailing edge, the more significant the improvement in total efficiency. However, when $x_r \le 0.3L_c$, the pump efficiency shows minimal changes with the jet hole position.

Comparing the dual-hole jet schemes $Case_{2.a}$ and $Case_{2.b}$, it is noted that under IGVF ≤ 0.2 conditions, the

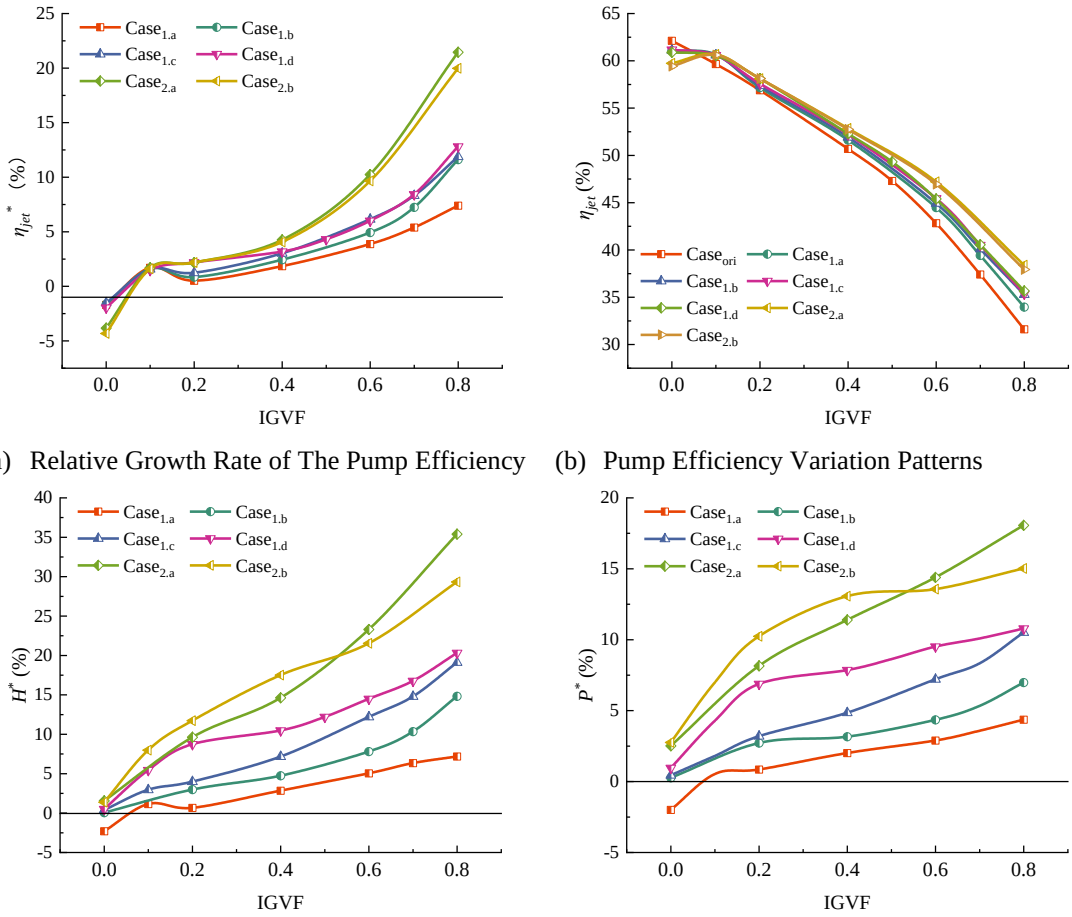

(a) Relative Growth Rate of The Pump Efficiency (b) Pump Efficiency Variation Patterns

(c) Relative Growth Rate of Head (d) Relative Growth Rate of Shaft Power

Fig. 6 Variation patterns of pump performance under different jet positions

pump efficiency differences between the two schemes are minor. However, at an IGVF of 0.4, the efficiency in $Case_{2.b}$ was significantly higher than that in $Case_{2.a}$. As the gas content continued to increase, the efficiency improvement in $Case_{2.b}$ gradually declined. At a 0.6 gas content condition, the pump efficiency improvement of $Case_{2.a}$ starts to exceed that of $Case_{2.b}$.

From this analysis, it can be concluded that when the jet hole is located within the range of 0.15 to 0.7L_c from the end of the blade, the net efficiency of the HAFM pump under gas–liquid mixed conditions improve. The closer the jet hole is to the end of the blade, the more significant the efficiency improvement. When the jet hole was located within the range of 0.15 to 0.3L_c from the trailing edge, the impact of the jet hole position on the pump efficiency decreased significantly. If the distance between the jet hole and the trailing edge is less than 0.15L_c, the improvement in the pump efficiency decreases.

By comparing the head and shaft powers for different jet positions in Fig. 6(c) and (d), it was found that the single-hole jet schemes have lower head and shaft powers than the dual-hole jet schemes. Comparing $Case_{1.a}$, $Case_{1.b}$, $Case_{1.c}$, and $Case_{1.d}$, it is evident that the closer the jet hole is to the blade trailing edge, the more significant the promotion in the head and shaft power of the HAFM pump. Comparing the dual-hole jet schemes $Case_{2.a}$ and $Case_{2.b}$, it is noted that when IGVF ≤ 0.4, the head and shaft power of the HAFM pump are higher, with jet holes placed closer to the blade's trailing edge. However, when IGVF ≥ 0.6, head and shaft power improvement is lower for schemes with jet holes closer to the end of the blade.

The active jet control strategy optimizes the original flow field by introducing external energy. The original energy carried by the jet was represented by the kinetic energy of the jet. Comparing the dual-hole jet scheme ($Case_{2.a}$) with the single-hole jet scheme ($Case_{1.d}$), after introducing an equal amount of jet energy, the external characteristics of the two schemes are shown in Fig. 7. The single-hole jet scheme is designated $Case_{1,}$ and the dual-hole jet scheme is named $Case_2$.

Comparing efficiency changes in the two schemes shows that under IGVF ≤ 0.2 conditions, the pump efficiency differences between the single and dual-hole jet schemes are not significant. However, as the IGVF increased, the net efficiency increase of the dual-hole jet scheme was significantly higher than that of the single-hole jet scheme. Figure 7 also shows that when 0.1≤IGVF ≤ 0.4, the head and shaft power of the single-hole jet scheme are higher than those of the dual-hole jet scheme. When IGVF ≥ 0.6, the head and shaft power of the dual-hole jet scheme exceed those of the single-hole jet scheme. This implies that the number of jet locations noticeably impacts the head and shaft powers of the HAFM pump. Comparing efficiency changes shows that the impact of jet

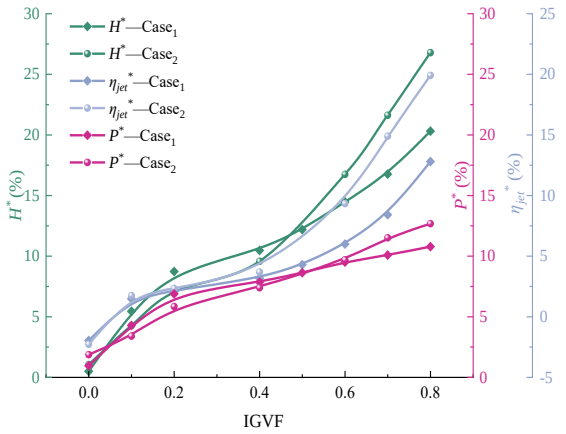

Fig. 7 Comparison of pump performance between single-hole jet and dual-hole jet under equal incident energy

location on head and shaft power of the HAFM pump varies with the initial IGVF. Overall, the dual-hole arrangement generally performs as well as, or better than, the single-hole arrangement in improving pump efficiency.

The analysis indicates that higher inlet gas volume fractions enhance the advantage of jet control in improving the pump efficiency. Conversely, under low-gas-volume conditions, the jet negatively impacts pump efficiency. The following section analyzes the mechanism of jet flow field control in relation to gas–liquid separation in a HAFM pump.

3.2 Internal Flow Characteristics of the Pumps with Different Jet Locations

3.2.1 Gas Phase Distribution Characteristics

Following flow separation in the impeller of the HAFM pump, the gas phase mainly accumulates in the flow channel near the hub side and the rear section of the impeller. Figure 8 shows the gas volume distribution on the developed surface of the blade cascade at 0.1 Span in the prototype pump impeller. As we can find that the gas volume fraction at the rear half of the impeller, i.e., the 0.5 to 1.0L_{imp} region, is noteworthily higher than in the front half of the impeller. The following section focuses on the 0.5 to 1.0L_{imp} region of the impeller to analyze the gas accumulation at different blade heights under different jet locations. As shown in Fig. 8, the 0.5 to 1.0L_{imp} (i.e., the impeller outlet) region was axially divided into equal intervals of 0.1L_{imp}. Gas accumulation in each region under different jet location schemes was compared and analyzed.

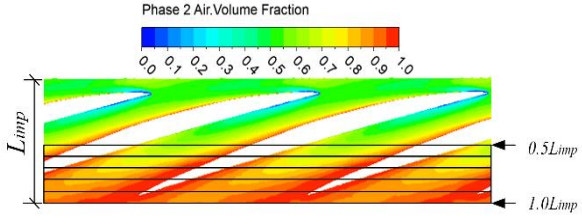

Fig. 8 Schematic of region division

The gas phase aggregation degree λ is defined to depict the degree of gas phase aggregation, and its expression is:

$$\lambda = \frac{S_{x,GVF>0.9}}{S_x} \times 100\% \quad (20)$$

where $S_{x,\,GVF>0.9}$ is the region where GVF exceeds 0.9, and S_x is the total region.

A comparison of the external characteristics shows that under active jet control, the increase in the total efficiency of the pump is especially noticeable at high initial gas volume fractions. Gas phase aggregation under different jet locations was analyzed under an IGVF of 0.6, and the mechanism of the pump net efficiency improvement was analyzed, examining how jet position influences gas-phase distribution and impacts pump efficiency. To intuitively analyze the effect of jet position on gas-phase aggregation, the change in the gas aggregation degree λ^* was used to compare aggregation before and after jet intervention. The expression for the change in gas phase aggregation degree λ^* is:

$$\lambda^* = (\lambda_{jet} - \lambda_{ori}) / \lambda_{ori} \times 100\% \quad (21)$$

Figure 9(a)–(c) show the changes in gas phase aggregation degree at different axial spans of the impeller (x = 0.5 L_{imp} to 1.0L_{imp}) within regions with axial spans of 0.1L_{imp} at 0.1, 0.3, and 0.5 Span. Figure 9 shows that the gas-phase aggregation degree varies significantly under different jet hole arrangements at the same Span flow surface. The closer the jet hole is to the impeller outlet, the more significant the reduction in the degree of gas-phase accumulation near the impeller outlet. The change in gas-phase accumulation degree at different Span flow surfaces varies by jet scheme, but each scheme shows a similar trend: the nearer to the middle flow surface along the blade height direction, the closer the position of the maximum reduction in the level of gas-phase accumulation is to the blade outlet. This occurs due to a radial velocity component, where the jet moves from the inlet to the outlet of the impeller while also moving from the hub side to the middle flow channel. The region with reduced gas-phase aggregation coincides with the area where the jet passes.

Figure 9 also shows that the gas-phase aggregation degree change patterns within the impeller are similar for $Case_{1.a}$ and $Case_{1.b}$, $Case_{1.c}$ and $Case_{2.a}$, and $Case_{1.d}$ and $Case_{2.b}$. For simplicity, $Case_{1.a}$ and $Case_{1.b}$ are referred to as scheme group 1#; $Case_{1.c}$ and $Case_{2.a}$ as scheme group 2#; and $Case_{1.d}$ and $Case_{2.b}$ as scheme group 3#. Since the jet holes in group 1# are located in the front section of the blade, their impact on air phase aggregation in the 0.5 to 1.0L_{imp} region is limited. Groups 2# and 3# consist of single- and dual-hole arrangements, respectively, with similar gas-phase aggregation patterns within each group. However, the second jet hole in the dual-hole scheme further reduces gas-phase aggregation in the more rearranged axial region of the impeller. A comparison of the two groups also shows that group 2# has a more significant reduction in the gas-phase aggregation degree than group 3#, and the single-hole jet scheme in group 2# is more effective in reducing gas-phase aggregation than

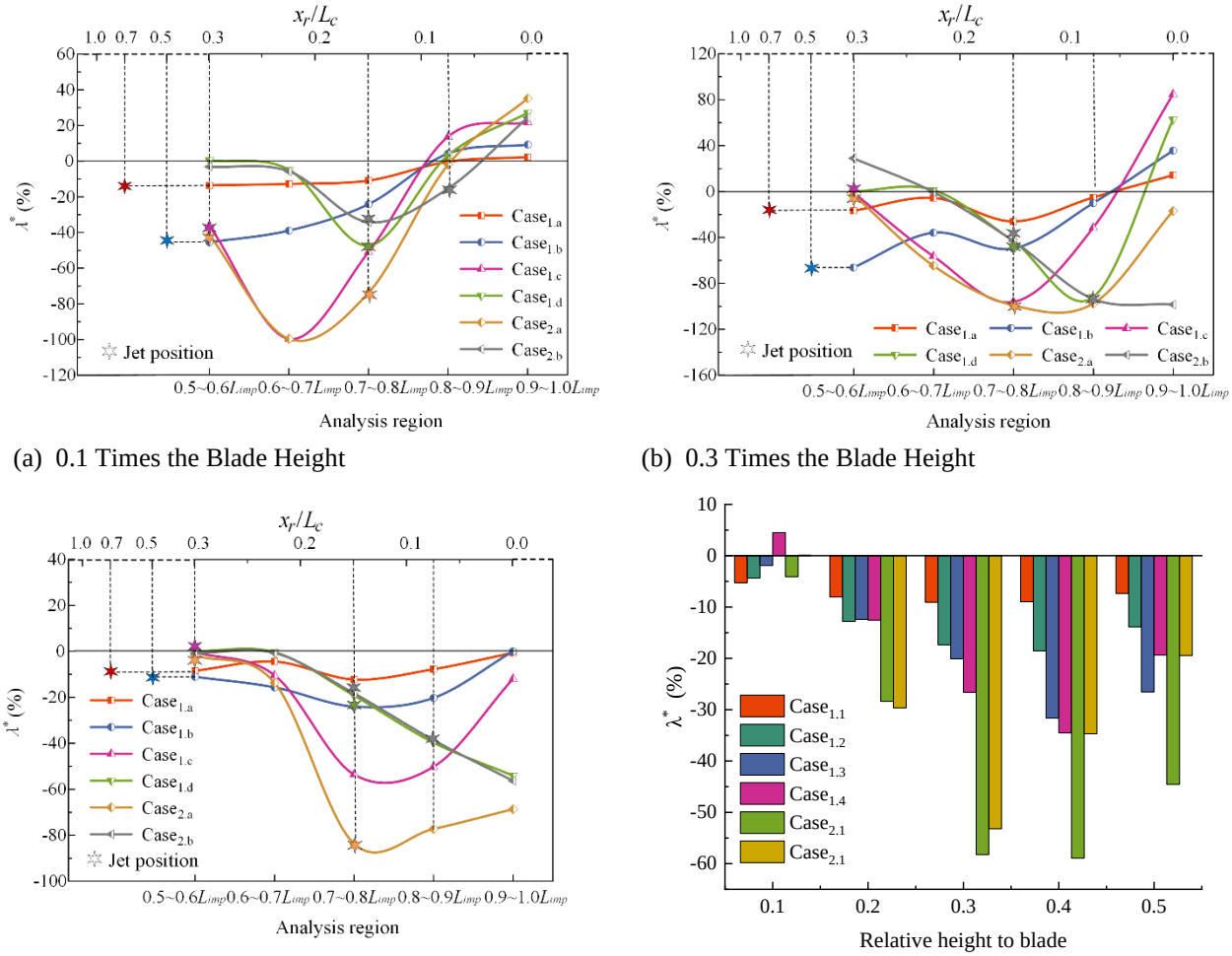

(a) 0.1 Times the Blade Height

(b) 0.3 Times the Blade Height

(c) 0.5 Times the Blade Height

(d) Total Region

Fig. 9 Gas phase distribution in multiphase pump impeller under different jet locations

the dual-hole scheme in group 3#. This indicates that placing the jet hole at the $0.3L_c$ position is the most effective in lowering air-phase accumulation within the impeller channel.

Due to the jet, the gas phase in the flow channel shifts from the downstream close to the jet position toward the outlet, ultimately aggregating in regions where the impact of jet lessens. This is reflected in Fig. 9 as a reduction in gas phase aggregation degree within the impeller compared to the original model, but with a higher gas phase aggregation degree in the 0.9 to $1.0L_{imp}$ region compared to the prototype model.

Since the jet holes extend to the front section of the impeller, Fig. 9(d) shows the changes in the degree of gas-phase aggregation within the impeller (0 to $1.0L_{imp}$) across the different flow surfaces. According to Fig. 9(d), the application of jet control contributed to a decline of the overall gas-phase content within the impeller. The dual-hole jet scheme is more effective than the single-hole scheme in reducing gas-phase aggregation. The closer the jet hole was to the blade's trailing edge, the less reduction in gas-phase aggregation near the hub. As the distance to the impeller outlet decreases, the gas content in the prototype pump increases, and the same jet energy has less impact in regions with higher gas volume fractions.

3.2.2 Gas Phase Velocity Characteristics

Figure 10 shows the gas phase velocity characteristics at 0.1 Span flow surface of the rotor at a 60% IGVF condition for the original and different jet location schemes. The velocity vector diagram of the prototype scheme shows that liquid flow exiting the blade pressure surface recirculates around the blade's trailing edge under an adverse pressure gradient at the impeller outlet, flowing back in the reverse direction. The high-speed reverse flow moves along the blade suction surface toward the impeller inlet until it dissipates energy by colliding with the forward flow, followed by the main flow along the outer edge of the recirculation zone and exiting the impeller.

From the streamlines of the jet schemes, it is evident that the introduction of the jet control strategy effectively suppresses reverse recirculation near the blade cascade trailing edge. However, the suppression effect on the reverse flow varies significantly at different jet locations. This conclusion is consistent with those reported (Meng et al., 2020). Comparing various single-hole jet schemes shows that the nearer the jet hole is to the blade outlet, the smaller the scale of the recirculation region. In Case$_{1.d}$, the

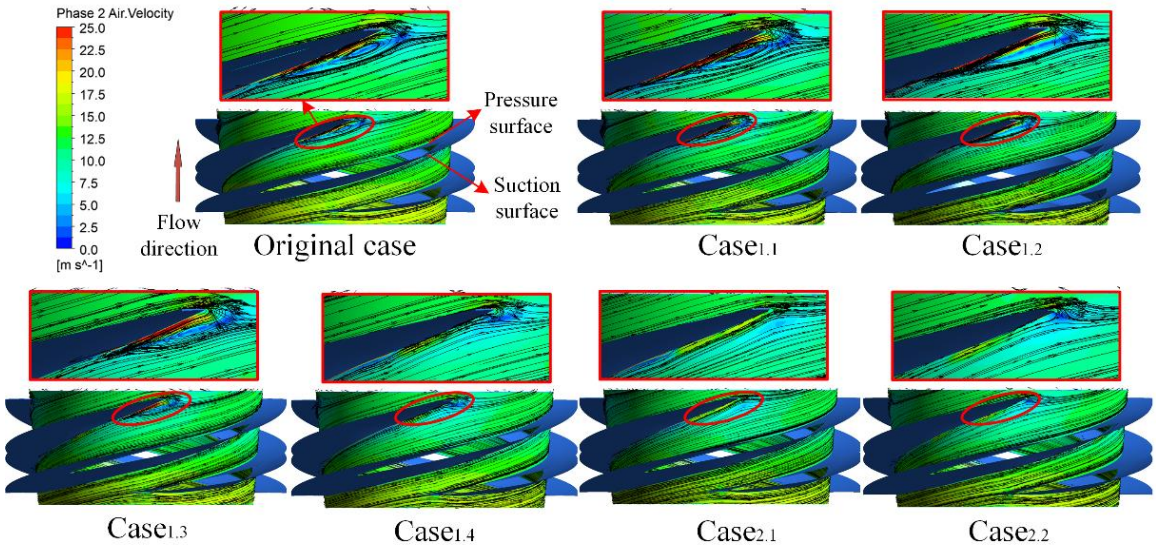

Fig. 10 Gas phase velocity at blade cascade trailing edge

recirculation area almost disappeared; however, a small wake region remained at the very end. Comparing the dual-hole jet schemes of $Case_{2.a}$ and $Case_{2.b}$, the flow at the blade cascade trailing edge is smoother in $Case_{2.a}$, whereas $Case_{2.b}$ exhibits a noticeable axial recirculation trend at the blade cascade leading edge, forming a low-velocity gas-phase zone. This phenomenon is similar to the trend observed by Meng et al. (2020) in single-hole jet schemes, where it was noted that when the jet hole was positioned further back, an end wall wake appeared downstream of the jet hole. The jet hole position at which the wall end wake occurs was $0.15L_c$ from the blade trailing edge. From the flow characteristics of schemes #1 and #2 in this study, it is known that the jet hole position when the end wall wake occurs is $0.075L_c$, which is further back than the position stated in reference. Due to the differences in the airfoil shape and inertia of the flow medium between this study and the reference, the specific positioning of the jet hole where the end wall wake occurred may differ from that in the reference; however, the overall trend remains consistent.

A comparison of the air-phase velocity characteristics under the single-hole jet schemes reveals that the closer the jet location is to the blade trailing edge, the better the improvement in the outlet gas-phase flow. The dual-hole jet schemes further demonstrate that the location of the jet hole cannot be infinitely close to the blade trailing edge. An optimal distance exists; if the distance is less than this optimal value, the improvement level of jet on the flow at the cascade trailing edge decreases.

3.2.3 Gas Phase Pressure Characteristics

Figure 11 presents the pressure characteristics on the impeller's flow surface at 0.1 Span under a 60% IGVF condition, comparing the original and various jet positioning schemes. The pressure contour distribution showed significant differences in the pressure gradient at the blade trailing edge among the various schemes. A more substantial pressure gradient indicates a greater flow resistance for the air phase at the blade trailing edge after gas–liquid separation in the impeller of HAFM pump under an adverse pressure gradient, making it more prone to deceleration, stagnation, and recirculation. Compared to the prototype scheme, the schemes with jets at specific locations exhibit a reduced pressure gradient at the blade cascade trailing edge. This phenomenon helps to improve the flow state near the suction surface of the blade at the impeller outlet and alleviates gas-phase retention near the outlet flow region.

A comparison of the single-hole jet schemes reveals that $Case_{1.a}$ and $Case_{1.b}$ show minimal changes in the pressure gradient compared with the prototype scheme, whereas $Case_{1.c}$ and $Case_{1.d}$ exhibit a significant reduction in the pressure gradient. The dual-hole jet schemes showed different pressure gradient along the extended direction of the blade profile line, with $Case_{2.a}$ showing a smaller pressure difference from the high-pressure surface to low-pressure side of the blade at the intersection with the trailing edge. Thus, the distribution of jet locations significantly affected the pressure gradient near the blade cascade trailing edge. Appropriately positioned jet holes can effectively decrease the pressure gradient at blade cascade trailing edge, providing favorable conditions for enhancing the gas-phase flow state at the impeller outlet.

To further analyze the impact of the jet position on the pressure of the HAFM pump, it is necessary to compare and analyze the blade load distribution between the prototype scheme and different jet position scheme. Because the jet points in the jet schemes were arranged starting at 30% of the blade length from the leading edge, the blade surface pressure values beyond 20% of the streamline direction were extracted for analysis. Figure 12 shows the surface pressure difference distribution at 0.1 Span for different schemes. The figure demonstrates the significant differences in the blade surface load distribution at different jet positions. Overall, the pressure difference along the streamline direction exhibited a similar pattern for the prototype scheme and single-hole jet schemes in $Case_{1.a}$, $Case_{1.b}$, and $Case_{1.c}$ (referred to as group 1# schemes below). Similarly, the pressure

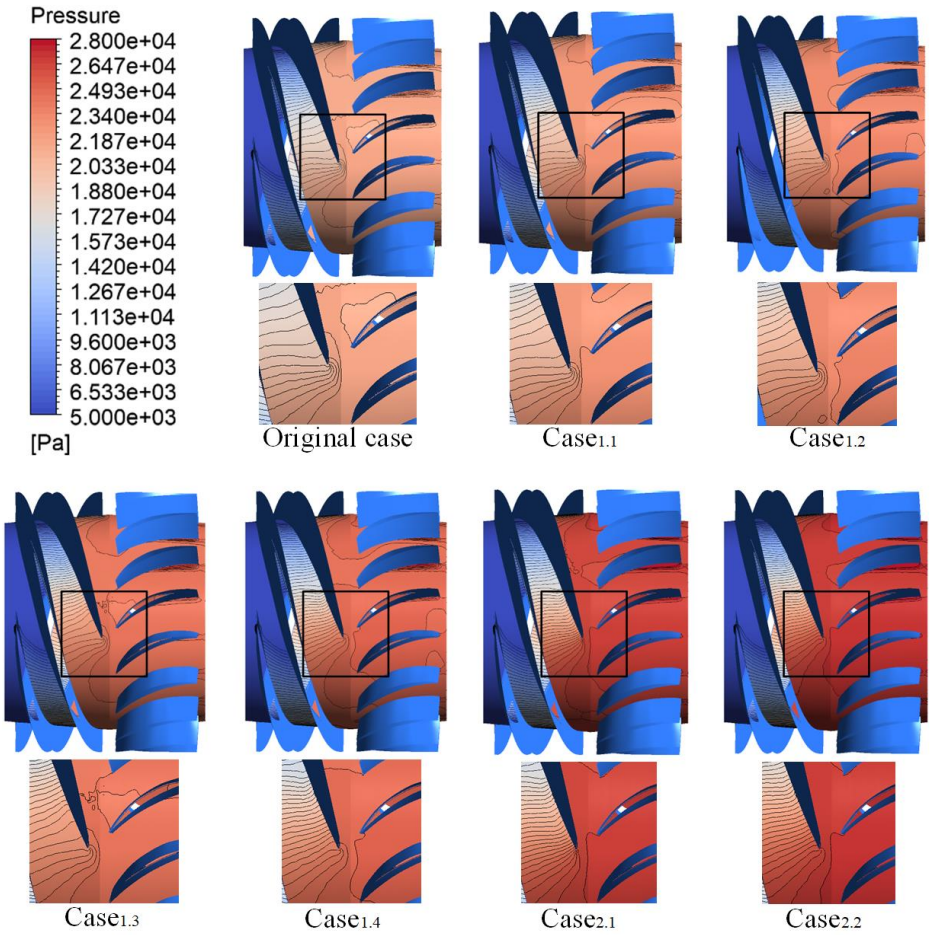

Fig. 11 Pressure gradient at cascade trailing edge

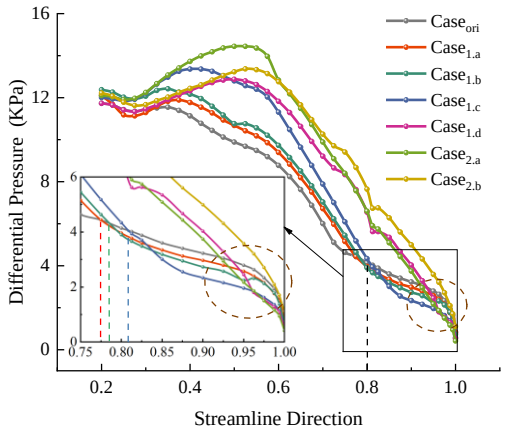

Fig. 12 Pressure difference distribution on blade surface

difference pattern in the streamline direction is similar for the single-hole jet scheme $Case_{1.c}$ and the dual-hole jet schemes $Case_{2.a}$ and $Case_{2.b}$ (referred to as group 2# schemes below).

Comparison of the group 1# schemes shows that the addition of jets raises the pressure difference in the 0.3–0.8 region along the streamline direction. Also, the closer the jet hole is to the blade outlet, the more significant the pressure difference from the high-pressure surface to low-pressure sides. However, in the 0.8–1.0 (approximation) range along the streamline direction, the pressure difference in the jet schemes decreases compared to the prototype scheme, and the closer the jet hole is to the blade outlet, the more noticeable the pressure difference reduction. A more significant difference in pressure from pressure to suction sides of the blade increases its working capacity. However, near the blade outlet, a larger pressure difference increases the likelihood of recirculation. This is because low-energy fluid clusters formed from the gas–liquid separation exist on the low-pressure side of the blade at the impeller outlet. Under large pressure differences, the outlet fluid flows more easily from the pressure side around the trailing edge to the low-energy fluid on the suction side, causing recirculation. Therefore, reducing the surface pressure difference in the 0.8–1.0 (approximation) range along the streamline direction in group 1# jet schemes is more beneficial for alleviating the gas lock and blockage phenomena near the blade cascade trailing edge.

Comparing the schemes within group 2#, it is found that $Case_{2.a}$ has a larger pressure difference in the front region of the blade compared to $Case_{1.d}$, while $Case_{2.b}$ has a larger pressure difference in the rear region of the blade. This is consistent with the relative positions of the jet holes in the three schemes. Furthermore, except for $Case_{2.b}$, the pressure difference from the high-pressure surface to low-pressure side of the blade near the blade outlet is lower in the other two schemes than in the prototype scheme. Based on the external characteristic features, the efficiency of $Case_{2.b}$ is also lower than that of $Case_{2.a}$.

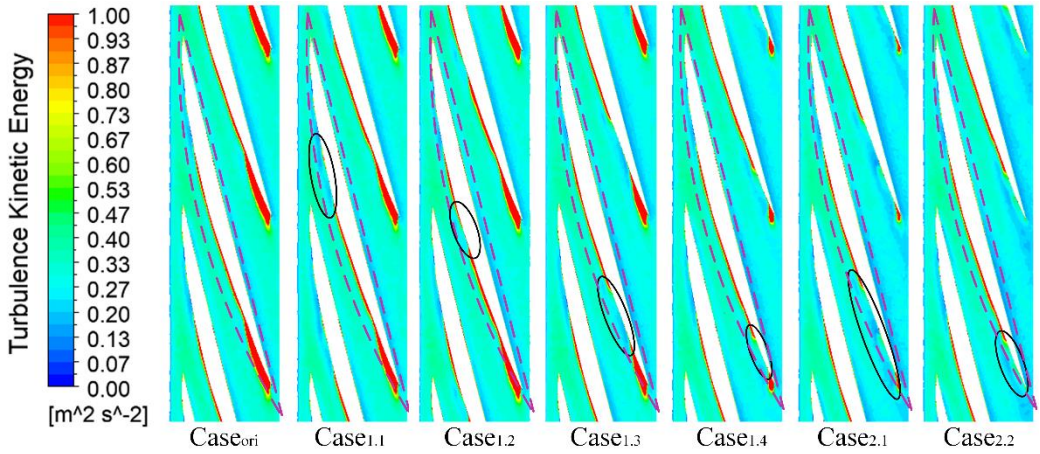

Fig. 13 Turbulent kinetic energy at 0.1 blade height flow surface

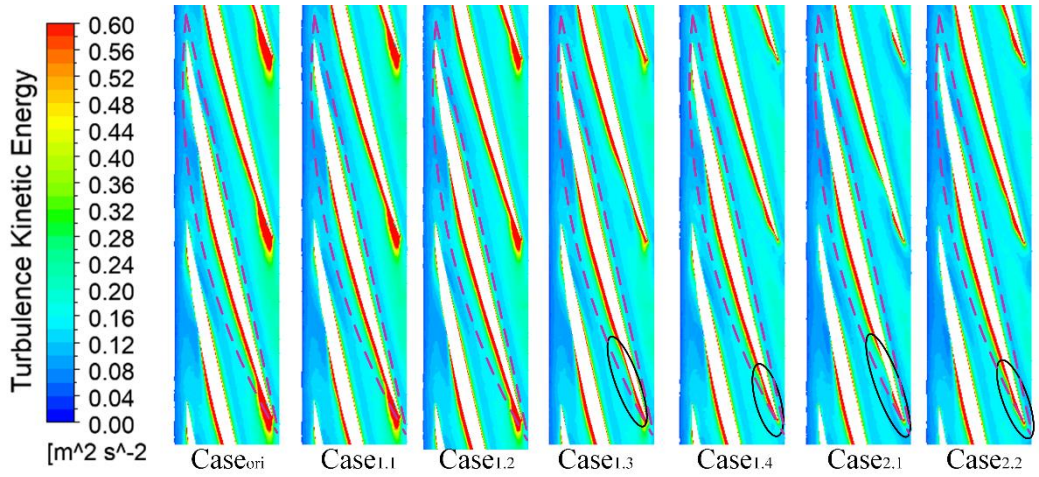

Fig. 14 Turbulent kinetic energy at 0.5 blade height flow surface

It is evident that the location of the jet holes affects the blade load distribution pattern, and surface pressure difference near the blade cascade trailing edge substantially influences the flow state in this region, thereby affecting the pump efficiency.

3.2.4 Turbulent Kinetic Energy Distribution Patterns

Figure 13 and Fig. 14 show the turbulent kinetic energy characteristics at 0.1 and 0.5 Span flow surfaces in the impeller under a 60% inlet gas volume fraction for the original case and various jet location cases. Turbulent kinetic energy mainly originates from the Reynolds shear stress on the time-averaged flow to supply energy to the turbulence. The magnitude of the turbulent kinetic energy represents the intensity of fluid velocity fluctuations. The greater the turbulent kinetic energy, the more chaotic the flow, resulting in greater fluid energy loss and a corresponding decrease in hydraulic efficiency.

From Fig. 13 and Fig. 14, we can observe that with the introduction of the jet control measures, the turbulent kinetic energy near the blade flow channel, particularly near the blade suction side, significantly decreased. The region of decreased turbulent kinetic energy on the blade suction side coincides with the location of jet hole. The dual-hole jet scheme in the region Case2.a of decreased turbulent kinetic energy on the blade lwo-pressure side fully covers the combined effect regions of Case1.c and Case1.d. Comparing Fig. 13 and Fig. 14, the region of decreased turbulent kinetic energy at 0.5 Span flow surface is closer to the blade trailing edge compared to the condition at 0.1 Span. Therefore, when the jet hole is too close to the blade outlet edge, the projection area of the jet effect in the blade height direction is narrow, indicating that the high gas-phase aggregation region near the middle flow surface of the flow channel will not be affected by the jet. The hydraulic loss pattern caused by gas–liquid separation in this region did not improve, thereby affecting the efficiency improvement under jet action, as seen in Case2.b. In Case2.b, the effect of the rear jet hole was weak; therefore, compared to Case2.a, the efficiency improvement of the pump decreased. Thus, from the changes in turbulent kinetic energy, it can also be observed that the jet location should not be overly near to the blade trailing edge.

4. CONCLUSION

This study employed jet flow field control technology, introducing external energy to actively intervene in the inner flow of the pump and reconstruct the inner flow field of a HAFM pump. By comparing the impact of changing jet locations on the gas-phase aggregation phenomena within the pump, this study explores the effect of the jet location on optimizing the

performance of a HAFM pump from the perspective of an adverse pressure gradient and recirculation improvement at the rotor cascade trailing edge. The following conclusions were drawn:

1) When the distance between the jet hole and the blade outlet edge is greater than $0.5L_c$, the closer the jet location is to the blade outlet, the more conspicuous the improvement in the pump performance. When the distance is $0.15L_c$ to $0.5L_c$, the influence of jet location on pump external characteristics is minor. When the distance is less than $0.15L_c$, the improvement in the head and efficiency under high gas volume fraction conditions decreases. When the jet hole is extremely close to the blade outlet edge, the turbulent kinetic energy in the middle region of the impeller flow passage is unaffected by the jet. In other words, the hydraulic loss caused by the gas–liquid separation phenomenon at this location is not improved, thereby affecting the efficiency improvement under the jet effect.

2) The change in the region of gas-phase aggregation was related to the jet hole location. Near the jet flow region, the gas-phase content changed significantly. The effect of reducing gas-phase aggregation varies with the jet hole location, with the most significant change occurring when the jet hole is at $0.3L_c$; the degree of gas-phase accumulation decreases the most, and the axial distribution range of the reduced area is the widest.

3) The effectiveness of jet control on the recirculation at the blade cascade trailing edge is closely related to the location of the jet flow. When the distance between the jet hole and the blade outlet edge is within $0.15L_c$ to $0.3L_c$, the recirculation area near the cascade trailing edge can be minimized to the greatest extent, thus optimizing the outlet flow conditions of the impeller. However, when this distance is less than 0.15Lc, a low-speed vortex forms at the intersection of the blade low-pressure surface and the trailing edge due to axial recirculation trends, resulting in high hydraulic-loss flow patterns.

4) The jet location affects the blade-surface load distribution pattern. The closer the jet hole is to the blade end, the more significant the load increase is before 80% of the blade length; however, the load on the blade surface decreases after 80%. When the blade working capacity is enhanced, the reduced pressure difference between the two sides of blades at the trailing edge can reduce the recirculation phenomenon and improve hydraulic efficiency.

ACKNOWLEDGMENTS

This study was supported by The National Natural Science Foundation of China (Grant Numbers 5217090851 and 52009051). The central Government Guides Local Science and Technology Development Fund Projects (23ZYQA0320).

CONFLICT OF INTEREST

The authors have declared that there are no potential conflicts of interest associated with this research. They affirm that neither personal nor financial relationships influenced the work, ensuring the objectivity and integrity of the study

AUTHORS CONTRIBUTION

Pan Qiang: Writing – original draft; Writing – review and editing; **Rennian Li:** Project administration; Supervision; Funding acquisition; **Wei Han:** Conceptualization; Funding acquisition; Supervision; **You Fu:** Methodology, Writing – review, and editing; **Sicong Zhang:** Investigation; Writing – review and editing.

REFERENCES

Benhmidene, A., Chaouachi, B., Bourouis, M., & Gabsi, S. (2011). Numerical prediction of flow patterns in bubble pumps. *Journal of Fluid Engineering-ASME, 133*, 1–8. https://doi.org/10.1115/1.4003664

Chang, Y., & Wang, X. (2024). Breakthrough innovations in deep sea and deep earth: Upholding our mission in increasing oil and gas reserves and production. *International Petroleum Economics, 32*(1), 42–44. https://lib.lut.edu.cn/asset/detail/0/2031258535823

Dehghan, A. A., & Shojaeefard, M. H. (2022). Experimental and numerical optimization of a centrifugal pump volute and its effect on head and hydraulic efficiency at the best efficiency point. *Proceedings of the Institution of Mechanical Engineers, Part C: Journal of Mechanical Engineering Science, 236*(9), 4577–4598. https://doi.org/10.1177/09544062211056019

Dehghan, A. A., Shojaeefard, M. H., & Roshanaei, M. (2024). Exploring a new criterion to determine the onset of cavitation in centrifugal pumps from an energy-saving standpoint; Experimental and numerical investigation. *Energy, 293*. https://doi.org/10.1016/j.energy.2024.130681

EI. (2023). *Statistical review of world energy 2023*. Energy Institute.

Ejim, C., Xiao, J., Lee, W., & Zabala, W. (2024). Performance envelope of a 538-series high-speed helico-axial pump for high-gas-volume-fraction operation. *SPE Journal*, 1–13. https://doi.org/10.2118/213740-PA

Guan, X. (2011). *Modern pumps theory and design* (1st ed.). China Aerospace Press.

Gundersen, T. Ø. S., Moënne-Loccoz, V., Dupoiron, M., Torbergsen, E. A., Balakin, B., Arntzen, B. J., & Hoffmann, A. C. (2023). Visualization of unsteady flow in a multistage helico-axial pump. *Journal of Fluid Engineering*, 1–13.

https://hdl.handle.net/11250/3106309

Han, W., Feng, H., Xu, Z., Hao, Y., Zhang, J., & Yang. C (2023). Effect of blade twist on the flow characteristics of gas-liquid two-phase flow in a spiral axial flow pump. *Journal of Applied Fluid Mechanics*, *16*(10), 1927–1937. https://doi.org/10.47176/jafm.16.10.1759

Han, W., Li, X., Su, Y., Su, M., Li, R., & Zhao, Y (2020). Effect of thickness ratio coefficient on the mixture transportation characteristics of helical–axial multiphase pumps. *Applied Sciences*, *10*(1), 345. https://doi.org/10.3390/app10010345

Han, W., Zhou, J., Li, R., & Ma, X (2023). Influence of trailing edge flap length and deflection angle on the performance of the multiphase pump. *Proceedings of the Institution of Mechanical Engineers, Part A: Journal of Power and Energy*. https://doi.org/10.1177/09576509231211395

Li, W., Li, Z., Han. W., Tan, S., Yan, S., Wang, D., & Yang, S (2023). Time-mean equation and multi-field coupling numerical method for low-Reynolds-number turbulent flow in ferrofluid. *Physics of Fluids*, *35*(12), 125145. https://doi.org/10.1115/1.4066486

Li, W., Li, Z., Han, W., Li, D., Yan, S., & Zhou, J. (2025). Study of the flow characteristics of pumped media in the confined morphology of a ferrofluid pump with annular microscale constraints. *Journal of Fluids Engineering*, *147*(2), 021201. https://doi.org/10.1063/5.0179961

Li, X., Liang, Z., Sun, P., Cui, X., & Liu, H. (2024). Numerical study on the effect of endwall adaptive jets on near stall performance of a transonic compressor. *Propulsion Technology*, 1–13. https://doi.org/10.13675/j.cnki.tjjs.2302026

Meng, Q., Chen, S., Liu, H., & Wang, S. (2020). Experimental study for effects of straight jets on flow field structure in a compressor cascade. *Propulsion Technology*, *41*(5), 1039–1045. https://doi.org/10.13675/j.cnki.tjjs.190306

Meng, Q., Du, X., Chen, S., & Wang, S. (2021). Numerical study of dual sweeping jet actuators for corner separation control in compressor cascade. *Journal of Thermal Science*, *30*, 201–209. https://doi.org/10.1007/s11630-019-1231-4

Menter, F. R. (1994). Two-equation eddy-viscosity turbulence models for engineering applications. *AIAA Journal*, *32*(8), 1598–1605. https://doi.org/10.2514/3.12149

Serena, A., & Bakken, L. E. (2015). Design of a multiphase pump test laboratory allowing to perform flow visualization and instability analysis. *Housing Studies*, *23*(6), 857–878. https://doi.org/10.1115/POWER2015-49769

Serena, A., & Bakken, L. E. (2016). *Flow visualization of unsteady and transient phenomena in a mixed-flow multiphase pump*. ASME Turbo Expo: Turbomachinery Technical Conference & Exposition. https://doi.org/10.1115/GT2016-56581

Shi, G., Liu, Z., Xiao, Y., Wang, Z., Luo, Y., & Luo, K. (2020). Energy conversion characteristics of multiphase pump impeller analyzed based on blade load spectra. *Renewable Energy*, *157*, 9–23. https://doi.org/10.1016/j.renene.2020.04.125

Situ, R., Hibiki, T., Brown, R. J., Hazuku, T., & Takamasa, T. (2011). Flow regime transition criteria for two-phase flow at reduced gravity conditions. *International Journal of Multiphase Flow*, *37*, 1165–1177. https://doi.org/10.1016/j.ijmultiphaseflow.2011.05.014

Suh, J. W., Kim, J. W., Choi, Y. S., Kim, J. H., Joo, W. G., & Lee, K. Y. (2018). Development of numerical Eulerian-Eulerian models for simulating multiphase pumps. *Journal of Petroleum Science and Engineering*, *162*, 588–601. https://doi.org/10.1016/j.petrol.2017.10.073

Wang, F. (2020). *Analysis method of flow in pumps & pumping stations*, first ed. China Water Power Press, Beijing, China.

Wang, W., Chu, W., Zhang, H., & Kuang, H. (2017). Experimental and numerical study of tip injection in a subsonic axial flow compressor. *Chinese Journal of Aeronautics*, *30*(3), 907–917. https://doi.org/10.1016/j.cja.2017.04.004

Wang, W., Liu, B., Lu, J., Feng, J., Chu, W., & Wu, Y. (2022). Comparative study of tip injection in a transonic and subsonic compressor. *Journal of Turbomachinery-Transactions of the ASME*, *144*(6), 061009. https://doi.org/10.1115/1.4053383

Wen, H., Tang, M., Lv, W., & Shi, G. (2024). Exploring the effect of the inlet gas volume fraction on the energy-conversion features of a multiphase pump using energy-transport theory. *Physics of Fluids*, *36*(4). https://doi.org/10.1063/5.0207041

Yan, D., Ye, J., Chen, M., & Shen, R. (2007). Pump sufficiency and conversion methods for efficiency. *Drainage and Irrigation Machinery*, *25*(1), 1–8. https://doi.org/10.3969/j.issn.1674-8530.2007.01.001

Yu, Y., Yu, F., Meng, R., Liu, H., Jiang, S., & Chen, H. (2018). The influence of endwall transverse jet on the performance of high-speed cascade. *Journal of Engineering Thermophysics*, *39*(9), 1921–1928. https://lib.lut.edu.cn/asset/detail/0/203338205686

Yu, Z. Y., Zhu, B. S., & Cao, S. L. (2015). Interphase force analysis for air-water bubbly flow in a multiphase rotodynamic pump. *Engineering Computations*, *32*, 2166–2180. https://doi.org/10.1108/EC-10-2014-0210

Zhang, W., Yu, Z., & Li, Y. (2018). Analysis of flow and

phase interaction characteristics in a gas-liquid two-phase pump. *Oil & Gas Science and Technology - Revue de l IFP, 73*(1), 11. https://doi.org/10.2516/ogst/2018072

Zhao, Z. (2023). *Research on end wall jet method and mechanism of stability enhancement in an axial flow pump* [Doctoral dissertation, Xi'an University of Technology]. https://doi.org/10.27398/d.cnki.gxalu.2023.001235

Zhou, J., Han, W., Li, R., Ma, X., Wang, H., & Li, W (2023). Flow control in multiphase pumps based on separated trailing edge flap. *Processes, 11*(11), 3066. https://doi.org/10.3390/pr11113066